NASA-TM-111974

50867

Spacecraft Jitter Attenuation Using Embedded Piezoelectric Actuators

W. Keith Belvin

NASA Langley Research Center

National Aeronautics and
Space Administration

Langley Research Center
Hampton, Virginia 23681-0001

SPACECRAFT JITTER ATTENUATION USING EMBEDDED PIEZOELECTRIC ACTUATORS

W. Keith Belvin
NASA Langley Research Center
Hampton, VA 23681-0001   USA

Abstract

Remote sensing from spacecraft requires precise pointing of measurement devices in order to achieve adequate spatial resolution. Unfortunately, various spacecraft disturbances induce vibrational jitter in the remote sensing instruments. The NASA Langley Research Center has performed analysis, simulations, and ground tests to identify the more promising technologies for minimizing spacecraft pointing jitter. These studies have shown that the use of smart materials to reduce spacecraft jitter is an excellent match between a maturing technology and an operational need. This paper describes the use of embedding piezoelectric actuators for vibration control and payload isolation. In addition, recent advances in modeling, simulation, and testing of spacecraft pointing jitter are discussed.

Introduction

Space offers a unique vantage point to observe the Earth and other planetary bodies. In order to achieve the desired spatial resolution, telescopes and other sensing instruments must be precisely pointed due to the vast distances between the spacecraft and the target to be observed. Unfortunately, disturbances cause unwanted excursions of the instrument boresight from the desired pointing direction. These excursions, called jitter, are a primary design driver for remote sensing spacecraft. To aid the spacecraft design, jitter levels are predicted using models to simulate the dynamic response caused by various disturbances. The simulation models include the spacecraft and its instruments, the attitude control system, and all known disturbances. These models are developed and refined as the spacecraft design matures. The jitter assessment is repeated whenever significant design changes occur.

The allowable pointing jitter is determined by orbital parameters, the measurement technique, and the desired data quality for each particular mission. Should jitter predictions indicate that pointing requirements would not be met, the spacecraft designer has several options. The first option is to reduce the disturbance forces and torques which create the pointing errors. This is sometimes successful but impractical for some missions. Second, the designer can negotiate with the data user to achieve a relaxed set of pointing requirements. While this frequently occurs, the compromised data quality may not be sufficient for some planned uses of the data.

The third option the designer may invoke involves changes to the spacecraft and its attitude control system. This option is usually expensive, particularly if it occurs late in the design of the spacecraft. Nevertheless, it is often the only viable way of achieving the required pointing jitter/stability.

The attitude control system bandwidth can be changed to improve pointing stability for low frequency disturbances ($\sim$ 1 Hz or less). Enhanced attitude control using feedforward compensation and multiple-input, multiple-output designs (e. g. Refs. 1-2) is beyond the scope of this paper and will not be further discussed herein. For other disturbances ($\sim$5 Hz or higher in frequency), changes in the structural design of the spacecraft bus and/or the measurement instrument can be made to lower the pointing jitter. These changes usually involve stiffness or other modifications for which a mass penalty is incurred. While such passive changes in the structural design are possible, they can create significant cost and schedule penalties in the spacecraft design. Moreover, such passive design changes also rely upon an accurate representation of the spacecraft/instrument dynamics and the disturbance profile. In this work, it is proposed that an alternative option be employed by the designer to reduce pointing jitter, namely, the use of smart materials.

The most natural application of smart materials for attenuation of vibrational jitter is to embed the materials directly in the load path of the structural system. For the spacecraft bus, this may be accomplished by replacing a truss member of the bus with a piezoelectric actuator. The embedded actuator permits electro-mechanical forces to be commanded in response to measured strain or acceleration for vibration control. Another important application of embedded actuators is for payload isolation. For example, piezoelectric actuators can be used to replace the kinematic mounts between the payload and the spacecraft bus.

This paper presents studies by the NASA Langley Research Center to assess modeling and hardware implementation issues associated with the use of piezoelectric actuators for vibration control and payload isolation. First, the substitution of a truss member with a piezoelectric actuator is presented to reveal some important modeling considerations. A simple laboratory test article is used for this study. Subsequently, the application of piezoelectric actuators for spacecraft jitter attenuation of the EOS AM-1 spacecraft is presented.

This work includes calculation of the spacecraft's jitter using preliminary design review (PDR) models and also development of a dynamics testbed for ground based, system level jitter studies. Test and analysis results show that the application of smart material systems for the reduction of spacecraft pointing jitter is quite viable.

Vibration Control Using Embedded Actuators

In 1988, NASA implemented a controls-structures interaction (CSI) technology program (Ref. 3) to improve the pointing performance of spacecraft. It was realized that uncertainties in flexible structure modeling, imperfect actuators and sensors, and the need for adaptable digital control were among the obstacles that had to be overcome. Thus, ground testbeds were put into operation to validate the technology on a system level prior to spacecraft application.

Active vibration control received extensive study in the CSI program and was validated using various ground testbeds. The excessive mass and volume of proof-mass (inertial) control actuators led to the search for alternative actuation devices. Since only relative forces are needed for flexible-body vibration control, smart materials were employed. This section describes a relatively simple testbed on which vibration control using piezoelectric actuators was successfully demonstrated. The actuators, modeling considerations and representative results are given along with some insights on the use of embedded actuators made of piezoelectric materials.

Ten Bay Truss Laboratory Model

A ten bay truss test article was constructed of erectable hardware designed under the CSI program (Ref. 4). As illustrated in Fig. 1, ten bays were configured into an L shape. Two bays were cantilevered horizontally from a backstop and 8 bays extended vertically. The bays are cubical with side dimensions of 10 inches. The individual struts or truss members are made of aluminum. Threaded steel rods are used to join the struts to the aluminum corner node balls. The test article also included six steel bars of 7 lbs each on the lower truss battens to represent non-structural payload mass.

The vibration control actuators consisted of piezoelectric "motors" and end fittings to adapt to the erectable hardware. The resulting "active members" could be used to replace any batten, longeron, or diagonal element of the truss. Commercially available Physik Instrumente piezo devices (Ref. 5) were used to assemble the active members. In the results that follow, two active members are located in the truss bay closest to the support, one as the lower horizontal member (longeron) and one as the adjacent diagonal member.

These locations were chosen using finite element models to determine regions of high strain energy.

Figure 2 shows a schematic of the primary parts of the piezoelectric active members. The actuators consist of a stack of individual piezoceramic disks encased in a stainless steel tube. When voltage is applied to each disk in the stack, they expand or contract in their longitudinal direction. By stacking the disks, a cumulative effect of the expansions and contractions can be exploited. Basic information for the longeron and diagonal active members are given in Table 1. The voltage command used to drive the active members was amplified by a two-channel model 50/750 high-voltage power amplifier form Trek, Inc. (Medina NY). This amplifier produces alternating-current voltages up to -1500 V at an average current level of 50 mA. To measure the vibrations, strain gages were mounted in series with the active members as indicated in Fig. 1. The strain gages were used for feedback and for performance assessment.
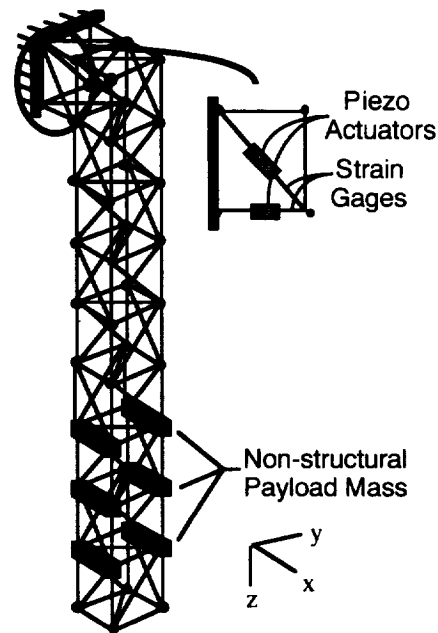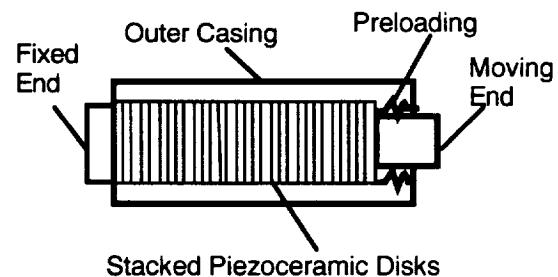

Fig. 1. Ten bay truss testbed schematic

Fig. 2. Piezoelectric "motor" schematic

2

Table 1 Piezoelectric actuator data

	Longeron	Diagonal
Model Number	P243.30	P243.40
Expansion at 1000V, (μm)	40	60
Max.Pushing Force, lb	6750	6750
Stiffness, lb/in	1.1992×10^6	0.7995×10^6
Resonant Frequency, Hz	4500	2200

Embedded Actuator Modeling Considerations

To simulate the dynamic response of structural systems with embedded actuators, the finite element method may be employed. A finite element representation for the actuator is first presented and then modeling of the structural system is discussed. It is shown that special care must be taken to include the effects of local deformations around the actuator when reduced order modeling is employed. The following sections describe the approach used to develop analysis models for this study.

Discrete Actuator Model
A simple finite element representation of the embedded actuator dynamics can be developed with the aid of Fig. 3 (Ref. 6). The governing equation is given in the form

$$\begin{bmatrix} m_e & 0 \\ 0 & m_e \end{bmatrix}\begin{Bmatrix} \ddot{r}_1 \\ \ddot{r}_2 \end{Bmatrix} + k_e\begin{bmatrix} 1 & -1 \\ -1 & 1 \end{bmatrix}\begin{Bmatrix} r_1 \\ r_2 \end{Bmatrix}$$
$$+ c_e\begin{bmatrix} 1 & -1 \\ -1 & 1 \end{bmatrix}\begin{Bmatrix} \dot{r}_1 \\ \dot{r}_2 \end{Bmatrix} = \begin{Bmatrix} -f_c \\ f_c \end{Bmatrix} + \begin{Bmatrix} f_1 \\ f_2 \end{Bmatrix} \tag{1}$$

Equivalent properties of the piezoelectric actuator are defined by

$$m_e = m / 6;$$
$$k_e = k^d - ch^2$$
$$f_c = chv$$

where the actuator structural mass is m, stiffness is k^d, and c_e is an estimated damping value. For a piezoelectric element, the stiffness k^d is measured with the electric circuit open. Coefficient h is the piezoelectric force/charge constant, c is the capacitance when the actuator is clamped, f_1 and f_2 are applied mechanical forces, and v is the applied voltage. When the actuator is coupled to the structure, the actuator displacements r_1 and r_2 are restricted to move with the structure and the applied forces are constraint forces to keep them together. For simulation, the actuator mass m is considered part of the structural mass.
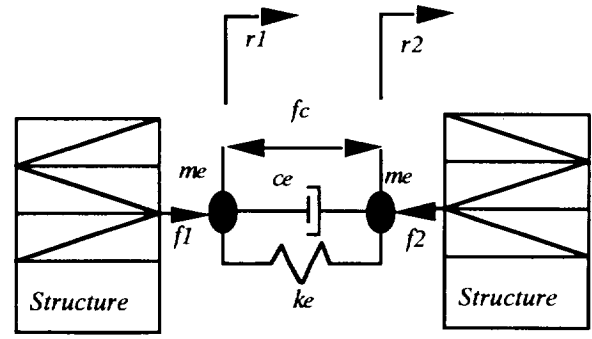

Fig. 3. Simplified representation of embedded piezoelectric actuator.

System Level Model Reduction
Using a finite element representation of the structure to be controlled, the system equations and physical output equations can be written as

$$M\ddot{r} + D\dot{r} + Kr = Eu \tag{2a}$$

$$\begin{bmatrix} y_L \\ y_S \\ y_A \end{bmatrix} = \begin{bmatrix} H_L & 0 \\ H_S & 0 \\ 0 & H_A \end{bmatrix}\begin{bmatrix} r \\ \ddot{r} \end{bmatrix} \tag{2b}$$

where M, D, K, and E are the mass, damping, stiffness and influence matrices, respectively, and r and u are the physical displacement and input vectors, respectively. The output vector for the two testbeds reported herein consists of the following: y_L, which represents the angular displacements (arc-sec); y_S, the strain (in/in); and y_A the translational accelerations (in/sec^2). Note that H_L, H_S, and H_A, are output sensor location matrices. While the full order FEM usually captures both local and global behavior, reduced order FEM models often lose information about local deformations. This is particularly true when eigenvectors are used to form the reduced order basis. For structures with embedded actuators, the local deformation behavior around the actuators must be retained during model reduction.

To retain a description of the deformations near the actuators, static "Ritz" vectors can be appended to the eigenvectors to enrich the basis used for model reduction (Refs. 7-8). For each embedded actuator, a static displacement vector is computed. The static vectors result from opposing loads being applied at each end of the actuator. Then a reduced order basis can be formed from the eigenvectors and static Ritz vectors via

$$r = \bar{T}z,$$
$$\bar{T} = \begin{bmatrix} T_e & T_r \end{bmatrix} \tag{3}$$

where T_e are the eigenvectors and T_r are the Ritz vectors and z is the reduced order model displacement vector. This transformation when applied to Eq. (1a) yields

3

$$\bar{M}z + \bar{D}z + \bar{K}z = \bar{E}u \qquad (4)$$

where,

$$\bar{M} = \begin{bmatrix} T_e^T M T_e & T_e^T M T_r \\ T_r^T M T_e & T_r^T M T_r \end{bmatrix}, \quad \bar{D} = \begin{bmatrix} T_e^T D T_e & T_e^T D T_r \\ T_r^T D T_e & T_r^T D T_r \end{bmatrix},$$

$$\bar{K} = \begin{bmatrix} T_e^T K T_e & T_e^T K T_r \\ T_r^T K T_e & T_r^T K T_r \end{bmatrix}, \text{ and } \bar{E} = \begin{bmatrix} T_e^T E \\ T_r^T E \end{bmatrix}.$$

Equation (4) provides a suitable reduced order model for simulating structures with embedded actuators. It has the capability of capturing both local (near actuators) and global response characteristics.

To show the effects of including the static vectors, the modeling approach of Eq. (4) has been applied to the ten bay truss. Six eigenvectors and two static vectors (one for each embedded actuator) have been used in the finite element model reduction. Figure 4 shows the improved accuracy obtained by adding the Ritz vectors in the reduced order modeling. Without the static vectors, the zero at 5 Hz is missed completely. The addition of the static vectors greatly improves the accuracy, however, the computational efficiency is degraded because the sparsity of the $\bar{M}$, $\bar{K}$, and $\bar{D}$ matrices has been lost.

It is computationally advantageous to reduce the bandwidth of $\bar{M}$, $\bar{K}$, and, if possible, $\bar{D}$. Since $T_e^T M T_e$ and $T_e^T K T_e$ are diagonal (from the eigen solution), bandwidth reduction must address the $T_e^T M T_r$, $T_e^T K T_r$, $T_r^T M T_e$, and $T_r^T K T_e$ terms of Eq. (4). In general these terms are fully coupled because the Ritz vectors are not orthogonal to the eigenvectors. However, the Gram-Schmidt formula for making vectors orthogonal can be used to make the Ritz vectors orthogonal to the mass weighted eigenvectors such that the $T_e^T M T_r$, $T_e^T K T_r$, $T_r^T M T_e$, and $T_r^T K T_e$ terms become null.

Let T_o be defined from T_e, T_r, and M using the Gram-Schmidt formula as

$$T_o = T_r - T_e T_e^T M T_r \qquad (5)$$

With this definition, the vectors, T_o, are orthogonal to the mass weighted eigenvectors. Hence, instead of using T_r directly, one uses T_o in the reduced order model basis

$$r = \hat{T}z,$$
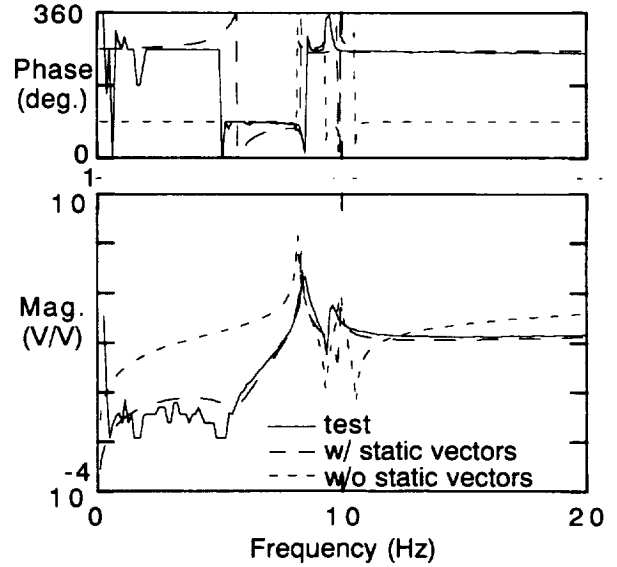$$\hat{T} = \begin{bmatrix} T_e & T_o \end{bmatrix} \qquad (6)$$

Fig. 4. Test and analysis comparison for two reduced order models

This transformation leads to

$$\hat{M}z + \hat{D}z + \hat{K}z = \hat{E}u \qquad (7)$$

where,

$$\hat{M} = \begin{bmatrix} I & 0 \\ 0 & T_o^T M T_o \end{bmatrix}, \quad \hat{K} = \begin{bmatrix} \Lambda & 0 \\ 0 & T_o^T K T_o \end{bmatrix}$$

$$\text{and } \hat{E} = \begin{bmatrix} T_e^T E \\ T_o^T E \end{bmatrix},$$

where Λ is a diagonal matrix containing the eigenvalues associated with the normal eigenvectors. If D is proportional to the Mass and/or Stiffness matrix, ($D = \alpha M + \beta K$), then

$$\hat{D} = \alpha \hat{M} + \beta \hat{K} \qquad (8)$$

NASTRAN routines can be used to extract the matrices Λ, $T_o^T M T_o$, $T_o^T K T_o$ and $\hat{T}$ directly from the finite element model. From these, $\hat{M}$, $\hat{K}$ and $\hat{E}$ can be formed as in Eq. (7) to produce a linear representation of a structural system with embedded actuators.

Dynamic Simulation and Jitter Analysis A very efficient software package has been developed to simulate systems of the form given in Eq. (7). The code, called PLATSIM (Refs. 9-10), converts Eqs. (7) and (2b) to the first order form

$$\begin{bmatrix} z \\ \dot{z} \end{bmatrix} = \begin{bmatrix} 0 & I \\ -\hat{M}^{-1}\hat{K} & -\hat{M}^{-1}\hat{D} \end{bmatrix} \begin{bmatrix} z \\ \dot{z} \end{bmatrix} + \begin{bmatrix} 0 \\ \hat{M}^{-1}\hat{E} \end{bmatrix} u \qquad (9)$$

4

$$\begin{bmatrix} y_L \\ y_S \\ y_A \end{bmatrix} = \begin{bmatrix} H_L \hat{T} & 0 \\ H_S \hat{T} & 0 \\ -H_A \hat{T} \hat{M}^{-1} \hat{K} & -H_A \hat{T} \hat{M}^{-1} \hat{D} \end{bmatrix} \begin{bmatrix} z \\ \dot{z} \end{bmatrix} + \begin{bmatrix} 0 \\ 0 \\ H_A \hat{T} \hat{M}^{-1} \hat{E} \end{bmatrix} u$$

(10)

The software uses sparse matrix coding and solution sequences to avoid unnecessary calculations. The model reduction approach presented above maintains the sparsity of the structural modal equations with only the $T_o^T M T_o$ and $T_o^T K T_o$ being nonsparse if D is proportional. Fortunately, these terms are of a size proportional to the number of actuators which is usually small compared to the number of modes retained in the model reduction. Hence, much of the sparsity due to the eigensolution can be utilized.

The PLATSIM code also models the attitude control system torques such that both flexible- and rigid-body closed-loop response can be simulated. In addition, an option for post processing of the simulation time histories to calculate jitter is provided. This code has been used extensively on the EOS AM-1 spacecraft.

Ten Bay Truss Vibration Control Results

Digital controllers have been implemented on the ten bay truss to evaluate the effectiveness of embedded piezoelectric actuators for vibration control. The control laws were of the form

$$x_c(k+1) = A_c x_c(k) + B_c y(k)$$
$$u(k+1) = C_c x_c(k) + D_c y(k)$$

(11)

where x_c represents the controller states, y is the strain measurement, u is the voltage command to the actuator, and A_c, B_c, C_c, and D_c are the discrete controller matrices. The primary modes of interest for control were at 8.4 Hz and 9.5 Hz. These modes exhibited coupled torsion and bending behavior in two planes. The controllers were implemented with an update rate of 250 Hz.

The truss was excited with sinusoidal voltage commands to the diagonal (at 8.4 Hz) and to the longeron (at 9.5 Hz) active members for 4.5 seconds. Subsequently, the excitation ceased and either free decay was allowed for open-loop measurements or the control law was activated for closed-loop measurements.

Figure 5 shows test and simulated time histories of the diagonal strain gage for the open-loop system. The simulated results use the modeling approach previously described with six eigenvectors and two static "Ritz" vectors in the model reduction. The measured open-loop damping for the two modes was 0.18 and 0.4 percent, respectively.

Typical vibration control results can be seen in Fig. 6. The controller was designed as a single-input, single-output for both of the longeron and diagonal sensor/actuator pairs. The controller emulates a second-order spring-mass-damper system by using the nearly collocated strain gage sensor and piezoelectric actuator. The simulation results show the vibration decays by 90 percent in two cycles, however, the test results show beating of the two modes that was not predicted. This beating resulted in a slower closed-loop response than anticipated. Nevertheless, the actuators did provide an effective means of vibration control. More results for this laboratory model can be found in Ref. 11.
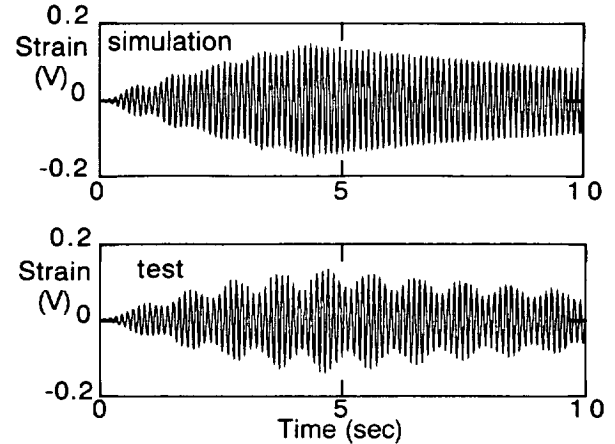

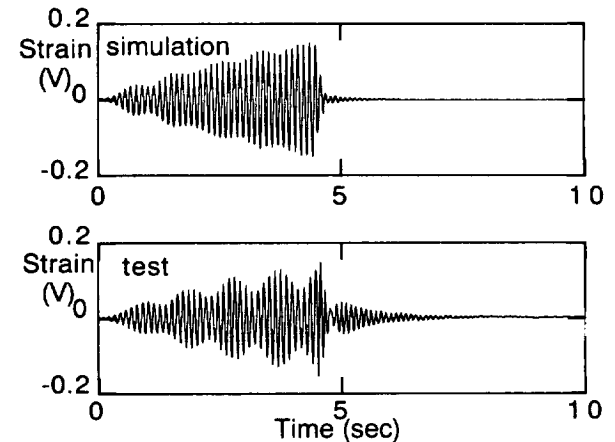Fig. 5. Test and simulation of ten bay testbed open-loop response

Fig.6. Test and simulation of ten bay testbed closed-loop response

Lessons Learned

Two important experiences occurred during this relatively simple vibration control investigation. First, the use of both eigenvectors and static "Ritz" vectors for model reduction of systems with embedded actuators was found to complicate the numerical computations. The dynamic frequency associated with the $T_o^T M T_o$ and $T_o^T K T_o$ terms in Eq. (7) is in general very high as these

terms represent local deformation behavior. The high frequency can lead to ill-conditioning and poor accuracy for some numerical integration algorithms. The reader is cautioned to be aware of this possible difficulty.

The second lesson involves the use of high voltage piezoelectrics. Laboratory experiences showed the power supplies necessary to provide sufficient voltage for the actuators would often saturate. When this condition occurred, very nonlinear behavior was observed. Even without saturation, significant amplifier dynamics were present. It is recommended that smart materials with lower operating voltages be employed when possible. The payload isolation results to be presented in the next section used 100 V piezoelectric "motors" for actuation. Above the 100 volt level, power switching electronics becomes quite large in size. Thus for spacecraft applications, it is recommended that embedded actuators be operated at voltages less than 100 V.

Payload Isolation Using Active Mounts

Payload isolation has also been investigated in the CSI program (Refs. 12-16). Usually, passive devices are employed to "decouple" a payload or disturbance source. The disadvantage of passive isolation is that low stiffness mounts are needed to obtain the proper dynamic coupling between the payload and the spacecraft. Low stiffness mounts can lead to large vibrations during launch and possible errors in the payload's pointing alignment with respect to the spacecraft. Hence, smart materials are being investigated to develop active isolation mounts for spacecraft payloads. The active mounts could maintain a high stiffness connection during launch and be actively softened when on-orbit. The following sections describe an investigation of payload isolation for the EOS AM-1 spacecraft.

EOS AM-1 Spacecraft Description

The EOS AM-1 spacecraft illustrated in Fig. 7 has five instrument systems (Ref. 17):

1. The Advanced Spaceborne Thermal Emission and Reflection (ASTER) radiometer. ASTER consists of three radiometers; visible and near infrared (VNIR), short-wave infrared (SWIR), and thermal infrared (TIR).
2. The Clouds and Earth's Radiant Energy System (CERES) scanning radiometers.
3. The Multi-Angle Imaging SpectroRadiometer (MISR)
4. The Moderate-Resolution Imaging Spectroradiometer (MODIS)
5. And the Measurements of Pollution In The

Troposphere (MOPITT) correlation spectrometer.

During the spacecraft design, dynamic response analyses were made to ascertain the pointing stability and jitter at each instrument's boresight location. Under a collaborative agreement between the NASA Goddard Space Flight Center (GSFC) and the NASA Langley Research Center (LaRC), LaRC investigated the use of payload isolation to reduce pointing jitter of the science payloads. In the study, the preliminary design review (PDR) disturbance, structural dynamics, and attitude control models were used to predict the dynamic response as discussed in the next section.

Fig. 7. Illustration of EOS AM-1 spacecraft

EOS AM-1 Spacecraft Jitter Simulation

In the PDR jitter assessment (which was performed with the aid of the PLATSIM code, Refs. 9-10), twelve disturbance events were used to determine the probable jitter amplitude. These disturbances include the CERES biaxial scan, MISR calibration, MODIS scan mirror imbalance, MOPITT scan operations, ASTER-SWIR pointing, ASTER-TIR chopper mechanism, ASTER-VNIR pointing, cryocoolers on MOPITT, ASTER-SWIR, and ASTER-TIR, reaction wheel assembly (RWA), and the solar array drive (SAD). For brevity, jitter amplitudes for only two instruments is presented herein; ASTER-SWIR and MISR. (The three ASTER radiometers will be referred to simply as SWIR, VNIR, and TIR in the remainder of the text.)

A graphical presentation of the pointing jitter simulation results is given in Fig. 8. The pointing requirements are given in arc-seconds. The root-sum-square (RSS) total of the individual disturbances shows that the pointing requirements are only marginally met. The primary disturbance events contributing to jitter were the VNIR pointing, the SWIR cryocooler, the CERES biaxial scan, and the SAD. The VNIR and SWIR Cryocooler disturbances are of a high frequency content whereas the
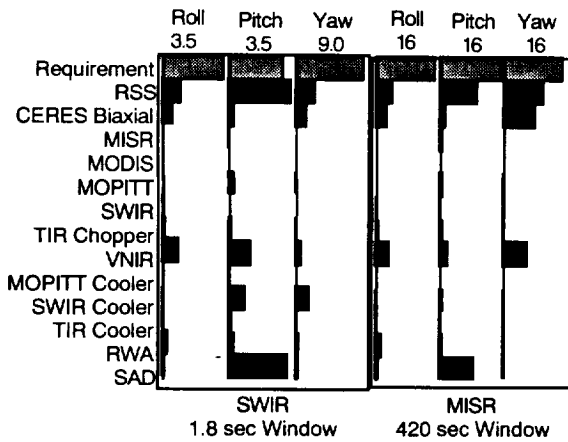
Fig. 8. Instrument pointing jitter/stability in arc-seconds

Fig. 9. Jitter response of SWIR (1.8 sec.) due to VNIR disturbance with active isolation

CERES and SAD primarily excited rigid-body and solar array response. Thus, payload isolation was evaluated for the ASTER-SWIR instrument as described below.

Payload Isolation

Since all instruments and equipment modules are interfaced to the EOS AM-1 spacecraft by kinematic mounts, the use of replacement isolator mounts is considered. The payload mounts are good candidates for isolation because they directly transmit the disturbances to/from the instruments. Kinematic mounts isolate local rotations from propagating into the science instrument payloads. They transmit no rotational torques. Hence, a properly designed isolator mount need only provide translational motion compensation to isolate the attached payload.

A key aspect of the isolator mount design undertaken in this study is to make them interchangeable with a normal (baseline) mount. This will provide the spacecraft designer flexibility to adapt to unanticipated dynamic requirements prior to launch. Jitter prediction is quite sensitive to modeling assumptions and disturbance frequency content. By making the isolator mounts interchangeable with baseline mounts, the designer would have the ability to replace one or more mounts if jitter predictions show low margins. Thus, active isolation mounts can be incorporated into the spacecraft design as late as the critical design review (CDR) with very little cost and schedule impact.

PLATSIM based analysis of the EOS AM-1 spacecraft indicated the VNIR disturbance produced about 1 arcsec/1.8 sec. of jitter in all three axes of SWIR. In the simulation model, the SWIR and VNIR mounts were made active by embedding a piezoelectric actuator in series with the kinematic mounts. Strain and strain rate feedback were used to help isolate the VNIR disturbance and the SWIR instrument. Simulations showed a simple low pass filter could significantly lower the pitch and yaw response of SWIR as shown in Fig. 9. The SWIR
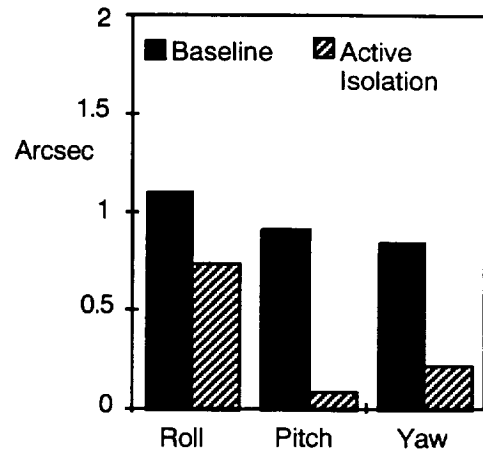
roll response is reduced by only 30 percent because there is significant rigid-body motion about the roll axis which cannot be mitigated by the isolation system. As an aside, the MISR instrument response was also reduced by about 10 percent.

The simulations showed that for the EOS AM-1 application, less than 5 microns stroke and 15 lbs of force were required by the isolation mounts. These force and stroke levels are easily obtained using commercial piezoelectric stack actuators. Thus isolator mounts, made with embedded piezoelectric elements, appear to provide a viable instrument or disturbance isolation system for EOS class payloads. To experimentally validate the simulation results, a dynamics testbed was assembled as described next.

EOS Dynamics Testbed

The EOS Dynamics Testbed (Ref. 18) is the fifth in a sequence of laboratory models developed at the NASA Langley Research Center in support of the CSI program. This testbed was created to develop and test precision pointing technologies associated with medium sized earth science and remote sensing platforms. The latest version of the testbed was designed to emulate the on-orbit dynamic behavior of the EOS AM-1 spacecraft.

Figure 10 shows the testbed which consists of a simulated spacecraft bus structure, two flexible appendages which represent the solar array and the high-gain antenna, dummy instrument and spacecraft subsystem masses, a suspension system to provide near free-free boundary conditions, three gimbaled instrument payloads, and instrumentation to quantify the dynamic response. The following paragraphs provide a description of the parts and characteristics of the testbed relevant to this study.
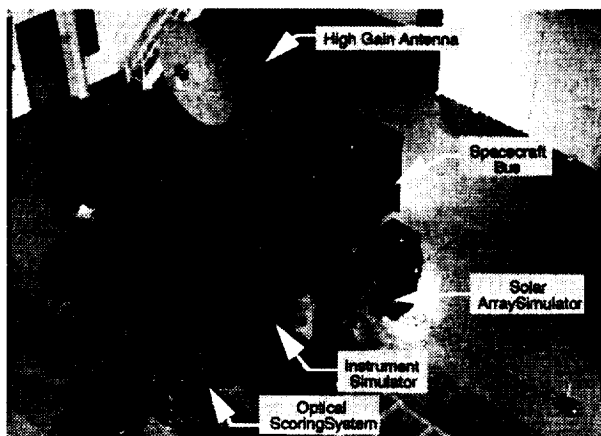
7

Fig. 10. LaRC EOS Dynamics Testbed

The simulated spacecraft bus is a truss structure built-up from 10 inch cubical bays. The geometry of the bus is approximately the same geometry as that of the EOS AM-1 spacecraft. However, due to limitations of the suspension system, the combined bus, payloads, and subsystems weight is approximately 1/10 the on-orbit weight of the EOS AM-1 spacecraft. Weight constraints produced a testbed with mass and stiffness characteristics scaling as 1/10 of full-scale, while geometry and frequency characteristics scale as unity. The first system bus natural frequency is 23 Hz and the first solar array natural frequency is 0.5 Hz. The testbed is suspended, from five cables, approximately 65 ft. below an over-head platform using pneumatic suspension devices. Near orbital boundary conditions are achieved since all six "rigid-body" mode frequencies are below 0.3 Hz.

Three instrument payloads simulate the actions of pointing or low-bandwidth scanning payloads. All three payloads are two axes gimbal devices. The payloads are positioned on the testbed at three locations representative of the EOS AM-1 spacecraft's TIR, MISR, and CERES instrument locations. Each is capable of pointing to within 2 arc-seconds with a bandwidth of approximately 8 Hz. One gimbal is rigidly attached to the bus (CERES location). Another gimbal is attached to the bus through a kinematic mounting system similar to that used on EOS AM-1 (TIR location). The third gimbal is mounted to the bus via isolator mounts that use piezoelectric actuators (MISR location).

Accelerometers are used to quantify the dynamics at the instrument/bus interface, and an optical scoring system (OSS) is used to quantify the pointing performance of the payloads. The accelerometers are arranged such that four are mounted on the gimbaled instrument interface plate, in line with each mount as shown in Fig. 11. An equal number of accelerometers are placed on the testbed interface plate, in line with each strut. The accelerometers have a resolution on the order of 10 micro-g's with a bandwidth of 150 Hz. The optical

measurement system is used to measure the roll and pitch angular displacement at the boresight of each instrument. These devices have a resolution of 0.2 arc-sec. and a bandwidth of 100 Hz.

Figure 12 shows a photograph of an instrument payload attached to the testbed with isolation mounts. Three of these mounts are commercial piezoelectric stack actuators, made by Polytec-PI, Inc., of Waldbronn, Germany. The fourth mount is a solid aluminum tube. Each piezoelectric actuator is instrumented with a strain gage sensor mounted on its internal piezoceramic stack to measure the total expansion and contraction. A built-in servo loop controller is used to help counter the hysteresis inherent in the piezoelectric actuators. The actuators are driven by a 3-channel Polytec-PI P-865.10 amplifier, capable of up to 100 V and 30 W output per channel. For these specific tests, the piezoelectric actuators are operated in the range of +/- 50 volts, to achieve up to 20 microns in expansion and contraction. Table 2 lists some of the pertinent characteristics of the piezoelectric devices used for payload isolation.
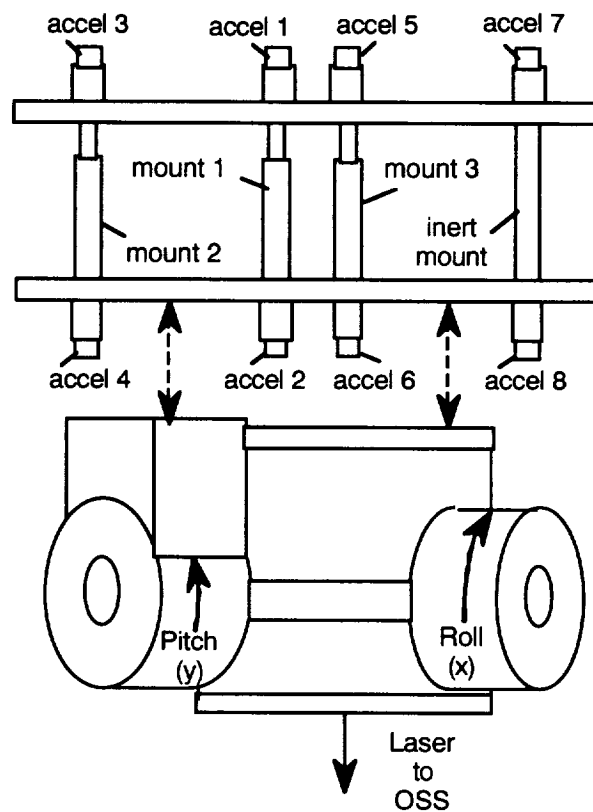

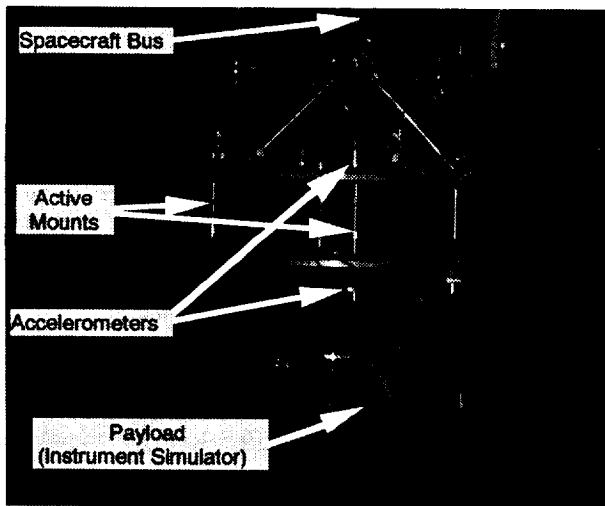Figure 11. Schematic of payload active isolator mounts on testbed

8

Fig. 12. Payload with active isolation mounts on testbed

Table 2. Piezoelectric actuator data for isolation

	Isolators
Model Number	P-845.37
Expansion at 100 V (μm)	40
Max. Pushing Force, lb	300
Stiffness, lb/in	3.8258×10^5
Resonant Frequency, Hz	9000

EOS Dynamics Testbed Isolation Results

The LaRC EOS Dynamics Testbed has been used for evaluation of various isolation concepts (Ref. 16). This section presents payload isolation results using the previously mentioned Polytec-PI devices for the isolation mount actuators.

While the objective of payload isolation is to reduce boresight pointing jitter of the payload, this measurement is not usually available for feedback. Hence the acceleration on the payload side of the isolator mount and the acceleration on the spacecraft bus side of the mount have been selected for feedback control (see Fig. 11). A simple two-zero, two-pole control law was used in conjunction with a bandpass filter in the feedback loop. A second order Butterworth filter was used with break frequencies at 20 and 60 Hz. The controller zeros were each set at 100 rad/s, whereas each controller pole was set to 1 rad/s. The controllers have been implemented digitally at an update rate of 1000 Hz.

The three active isolator mounts that support the payload have been controlled independently. Open-loop (baseline) and closed-loop (isolated) frequency response functions of Accelerometer # 6 due to an excitation at the SWIR cryocooler location is shown in Fig. 13. Using isolator mount # 3 (see Fig. 11), significant attenuation is achieved. It is noted that the bandwidth of

the isolators is approximately 45 Hz. Above this frequency, the compensator rolls off and the phase delay actually accentuates the response level. To determine the transmissibility across the interface, one can examine the ratio of open-loop acceleration (hard mounted) to closed-loop acceleration (isolated). Figure 14 shows the transmissibility using mount #3 and accelerometer # 6. These data show the isolation mounts do provide broadband performance.

Although the payload base acceleration levels are reduced, the most important metric is the payload's boresight jitter. Outputs of the optical scoring system with and without active isolation are shown in Fig. 15 for cryocooler-like disturbances. Just using a single isolator mount provides about 80 % reduction in pointing jitter. Figure 16 shows the same data in the image plane of the instrument. It is clear the isolation mounts can greatly improve spatial resolution. These results are very encouraging and have led to further plans for application of embedded piezoelectric actuators as described at the end of the next section.
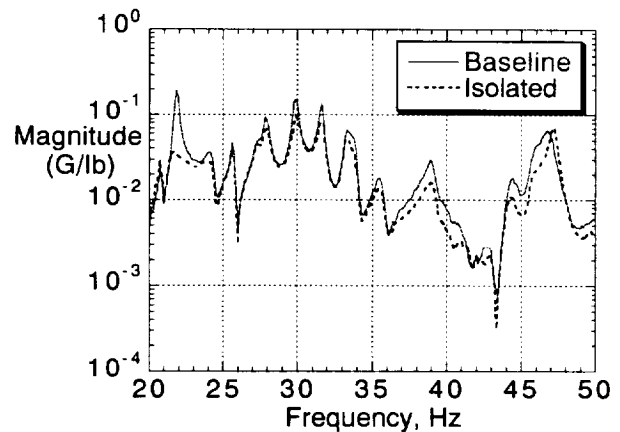

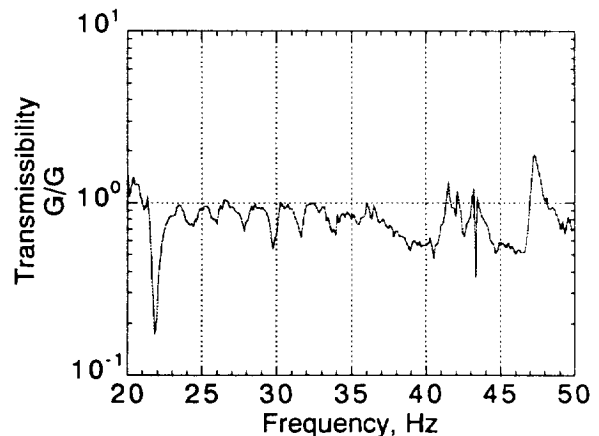Fig. 13. Frequency response of accelerometer 6

Fig. 14. Isolation mount acceleration transmission

9

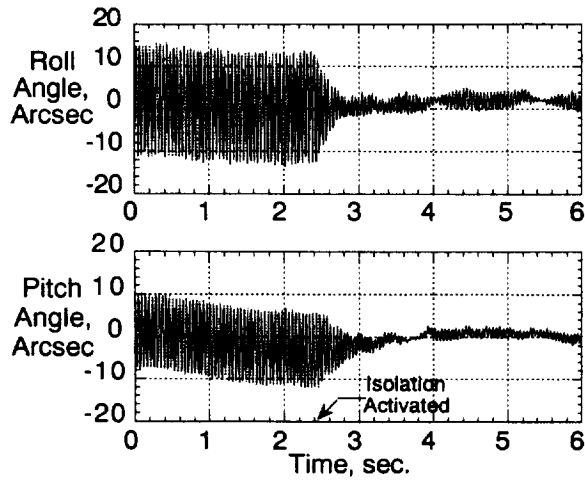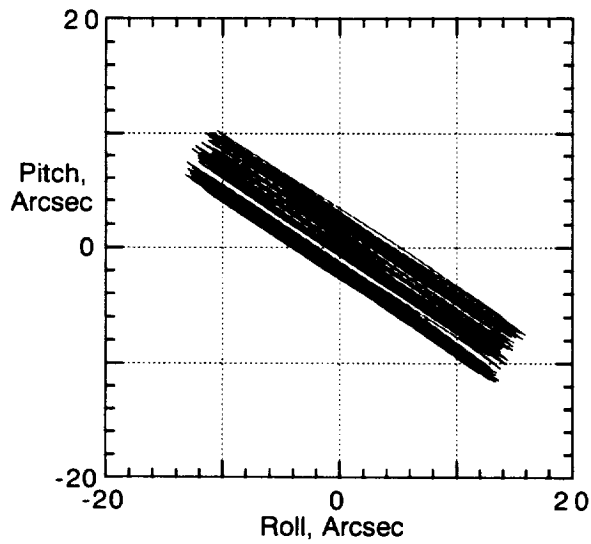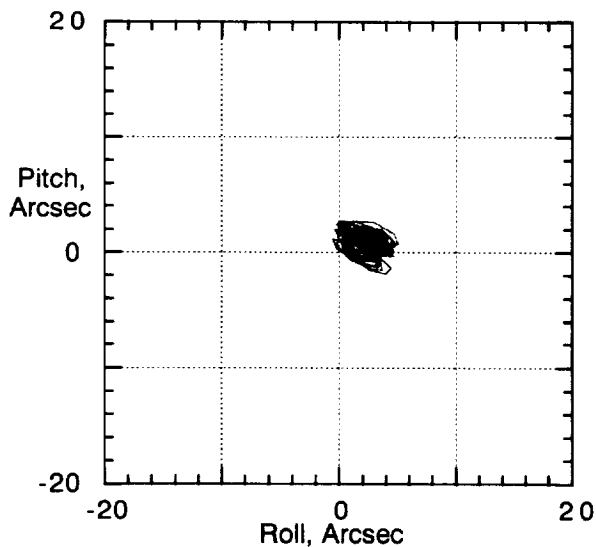Fig. 15. Payload boresight pointing, 22 Hz disturbance (isolation activated at t=2.4 sec)

a) Jitter without active isolation

b) Jitter with active isolation

Fig. 16. Instrument jitter due to 22 Hz disturbance

Summary and Future Directions

Developments in actuators and sensors made possible through smart materials research are beginning to find acceptance by the spacecraft community. In this study, the use of embedded actuators made from smart materials are employed to reduce instrument vibration, thereby, improving the quality of remote sensing data. Both vibration control and payload isolation have been investigated using piezoelectric stack actuators.

A simple ten bay truss structure was employed to investigate modeling and operation of embedded piezoelectric actuators. Vibration control results showed the importance of modeling local deformations near the actuator. A model reduction procedure was developed that maintains much of the sparsity associated with modal truncation and yet captures localized response. With this procedure, an efficient sparse matrix code has been developed and utilized to predict pointing jitter with very large simulation models.

The use of payload isolation via active isolator mounts between remote sensing instruments and the spacecraft has also been evaluated. These isolators can be implemented on spacecraft with relatively little impact on the existing design. Simulation of the proposed isolation technology on a real spacecraft, namely EOS AM-1, have shown up to 70 percent reduction in pointing error.

A large scale ground testbed is presented for the development of precision pointing technology. The LaRC EOS Dynamics Testbed provides near on-orbit boundary conditions and has instrument simulators for both pointing and scanning. The testbed is instrumented such that sub arc-sec angular vibrations can be measured for confirmation of system level jitter. Payload isolation tests have confirmed 50 to 80 percent reduction in payload pointing error when piezoelectric stack actuators are used to mount the instruments.

It is believed remote sensing spacecraft will soon need to employ active jitter control to meet ever increasing spatial resolution requirements. In addition, with the trend to smaller spacecraft, vibrational jitter of instruments is likely to increase due to the close proximity of disturbances and instrument optics. Since embedded actuators are so well suited to spacecraft jitter reduction, plans are to directly integrate vibration management into the spacecraft structure. These integrated structures are likely to also include thermal, power and data management functions as well. The NASA Langley Research Center plans to continue the development of low cost, lightweight approaches to reduce jitter on-board remote sensing spacecraft. Embedded actuators made of smart materials promises to be the leading candidate for this effort.

10

References

1. McLaren, M., Chu. P., and Price, X., "Control-Structure Interaction/Mirror Motion Compensation," NASA Contractor Report 189672, Sept. 1992.

2. Hughes, R., and Appleby, B., "Contingency Controller Study For The EOS-AM Attitude Control System," Martin Marietta Astro Space, June, 1993.

3. Newsom, J., Layman, W., Waites, H., and Hayduk, R., "The NASA Controls-Structures Interaction Technology Program," IAF-90-290, Oct. 1990.

4. Belvin, W. K., Elliott, K. B., Horta, L. G., Bailey, J., Bruner, A., Sulla, J., Won, J., and Ugoletti, R., "Langley's CSI Evolutionary Model: Phase 0," NASA TM-104165, 1991.

5. Physik Instrumente Catalog, GmbH & Co., Waldbronn, Germany.

6. Won, C. C. and Sulla, J. L., "Experiments on the Linearization of a Piezoelectric Strut," *Proceedings of the North American Conference on Smart Structures and Materials*, Vol. 2192, February 1994, pp. 168-175.

7. Kline, K. A., "Dynamic Analysis Using a Reduced Basis of Exact Modes and Ritz Vectors," *AIAA Journal*, Vol. 24, No. 12, December 1986, pp. 2022-2029.

8. Sandridge, C. A. and Haftka, R. T., "Modal Truncation, Ritz Vectors, and Derivatives of Closed-Loop Damping Ratios," *Journal of Guidance, Control and Dynamics*, Vol. 14, No. 4, July-August 1991, pp. 785-790.

9. Maghami, P. G., Kenny, S. P., and Giesy, D. P., "The PLATSIM Software Package: A Simulation And Analysis Tool For Large-Order Flexible Systems With Applications To EOS AM-1," *Proceeding of the 18th Annual AAS Guidance and Control Conference*, AAS 95-003, Keystone, CO, Feb. 1-5, 1995.

10. Maghami, P. G., Kenny, S. P., and Giesy, D. P., PLATSIM: An efficient Linear Simulation and Analysis Package for Large-Order Flexible Systems, NASA TP 3519, 1995.

11. Won, C. C., Sulla, J. L., Sparks, D. W., Belvin, W. K., "Application of Piezoelectric Devices to Vibration Suppression," *Journal of Guidance, Control, and Dynamics*, Vol. 17, No. 6, Nov.-Dec. 1994, pp. 1333-1338

12. Collins, S. A. and von Flotow, A. H., " Active Vibration Isolation for Spacecraft" *42nd Congress of the International Astronautical Federation*, Oct. 1991, Montreal, Canada, Paper No. IAF-91-289.

13. Lurie, B. J., Fanson, J. L., and Laskin, R. A.," Active Suspensions for Vibration Isolation," *Proceedings of the 32nd AIAA/ASME/ASCE/AHS/ASC Structures, Structural Dynamics, and Materials Conference*, MD, April 1991, AIAA Paper No. 91-1232, pp. 2256-2260.

14. Blackwood, G. H. and von Flotow, A. H., "Active Vibration Isolation for Controlled Flexible Structures," MIT Space Engineering Research Center, Report No. 13-93, Oct. 1993.

15. Swanson, D. A., Miller, L. R., and Norris, M. A., " Multi-Dimensional Mount Effectiveness for Vibration Isolation," *Proceedings of the 33rd AIAA/ASME/ASCE/AHS/ASC Structures, Structural Dynamics and Materials Conference*, TX., April 1992.

16. Belvin, W. K., Sparks, D. W., Horta, L. G., and Elliott, K. B., "On the Isolation of Science Payloads From Spacecraft Vibrations," *Proceedings of the 36th AIAA/ASME/ASCE/AHS/ASC Structures, Structural Dynamics, and Materials Conference*, New Orleans, LA, April 1995, AIAA Paper No. 95-1234, pp. 698-708.

17. Asrar, G., and Dokken, D., editors; "EOS Reference Handbook," NP-202, March 1993.

18. Gronet, M. J., Davis, D. A., and Tan, M. K., "Development of the CSI Phase-3 Evolutionary Model Testbed," NASA Contractor Report 4630, October 1994.